

Demonstration of fault-tolerant universal quantum gate operations

<https://doi.org/10.1038/s41586-022-04721-1>

Received: 26 November 2021

Accepted: 4 April 2022

Published online: 25 May 2022

 Check for updates

Lukas Postler¹, Sascha Heußen^{2,3}, Ivan Pogorelov¹, Manuel Rispler^{2,3}, Thomas Feldker^{1,4}, Michael Meth¹, Christian D. Marciniak¹, Roman Stricker¹, Martin Ringbauer¹, Rainer Blatt^{1,5}, Philipp Schindler^{1✉}, Markus Müller^{2,3} & Thomas Monz^{1,4}

Quantum computers can be protected from noise by encoding the logical quantum information redundantly into multiple qubits using error-correcting codes^{1,2}. When manipulating the logical quantum states, it is imperative that errors caused by imperfect operations do not spread uncontrollably through the quantum register. This requires that all operations on the quantum register obey a fault-tolerant circuit design^{3–5}, which, in general, increases the complexity of the implementation. Here we demonstrate a fault-tolerant universal set of gates on two logical qubits in a trapped-ion quantum computer. In particular, we make use of the recently introduced paradigm of flag fault tolerance, where the absence or presence of dangerous errors is heralded by the use of auxiliary flag qubits^{6–10}. We perform a logical two-qubit controlled-NOT gate between two instances of the seven-qubit colour code^{11,12}, and fault-tolerantly prepare a logical magic state^{8,13}. We then realize a fault-tolerant logical *T* gate by injecting the magic state by teleportation from one logical qubit onto the other¹⁴. We observe the hallmark feature of fault tolerance—a superior performance compared with a non-fault-tolerant implementation. In combination with recently demonstrated repeated quantum error-correction cycles^{15,16}, these results provide a route towards error-corrected universal quantum computation.

Quantum computers hold promise to efficiently solve important computational tasks that are beyond the capabilities of classical computers, such as prime factorization or the simulation of complex quantum systems^{17,18}. A digital quantum computer will offer a native gate set, which is composed of the operations that can be physically executed in hardware. Remarkably, finite sets of native gates are sufficient to compose any operation to an arbitrary desired precision, rendering such gate sets universal¹. A fundamental challenge is to keep the quantum computation coherent, but all components of the quantum computer, such as physical qubits, gate operations and measurements, are inherently prone to errors. This roadblock towards large-scale quantum computation can be lifted with the circuit design principle of quantum fault tolerance^{2–5}. The central idea is to use quantum error correction (QEC) codes, where many physical qubits together comprise so-called logical qubits such that the logical information is distributed non-locally and thereby protected from decoherence and errors owing to finite control accuracy. By ingenuity of code design, it thus becomes possible to suppress logical decoherence arbitrarily by adding redundancy, once the physical noise level falls below some threshold¹⁹. Arbitrary logical quantum computation demands that a universal logical gate set has to be synthesized from physical gates, which presents challenges. To prevent previously localized errors from spreading over the entire qubit register and destroying the computation, logical gates have to be designed with fault-tolerance

guarantees: for QEC codes with the potential to correct at least one arbitrary single error, this means that a single error occurring at any location (initialization, gate or measurement) in a particular circuit may under no circumstances turn into a non-correctable error on two or more qubits. When assuming for simplicity that every location has some error probability p , the logical failure rate without fault tolerance will scale as $p_L \propto Np$, with N the number of error locations in the circuit that lead to a logical error. Although adding further gates and qubits for fault tolerance increases the number of circuit locations, the logical failure rate will now scale with $p_L \propto N'p^2$, that is, it is quadratically suppressed in p , where N' now denotes the number of pairs of locations where two errors lead to a logical error. This entails one of the hallmark features of fault-tolerant (FT) implementations: despite adding more (noisy) qubits and gates, the quality of the encoded information can be improved, if the physical noise level is sufficiently low. Certain QEC codes facilitate an FT implementation of some gates by acting on all physical qubits individually—called a transversal logical gate. However, a universal gate set with all gates having a transversal unitary implementation is forbidden by a no-go theorem²⁰. This leads to the difficulty that to reach universal FT computation, at least one logical gate must be implemented by other means, such as magic-state injection¹⁴ or code switching²¹. Fulfilling fault-tolerance requirements for these approaches typically implies a substantial resource overhead²².

¹Institute for Experimental Physics, University of Innsbruck, Innsbruck, Austria. ²Institute for Quantum Information, RWTH Aachen University, Aachen, Germany. ³Institute for Theoretical Nanoelectronics (PGI-2), Forschungszentrum Jülich, Jülich, Germany. ⁴Alpine Quantum Technologies GmbH, Innsbruck, Austria. ⁵Institute for Quantum Optics and Quantum Information, Austrian Academy of Sciences, Innsbruck, Austria. ✉e-mail: philipp.schindler@uibk.ac.at

The growing experimental effort towards FT quantum computation has seen tremendous advances: non-FT logical state preparation and transversal single-qubit logical gate operations have been shown in a seven-qubit experiment with trapped ions²³, whereas non-FT two-qubit gates have been demonstrated in error-detection codes^{24,25}. State preparation of a topological surface code state²⁶, repetitive stabilizer measurements in an error-detecting surface code^{27,28} and exponential error suppression in a repetition code²⁹ have been demonstrated in superconducting architectures. Shortly following a theory proposal towards demonstrations of fault tolerance in small systems³⁰, experiments showed state preparation using error-detection codes and post-selection^{31–33}, and recently error correction for FT state preparation and an FT logical single-qubit Clifford gate³⁴. Theoretical studies have substantially reduced the resource requirements for fault tolerance by the concept of flag fault tolerance^{6–10}. Here dedicated auxiliary qubits are introduced, which signal the presence of dangerous errors. This concept was used to demonstrate FT operation of the five-qubit code in a nitrogen-vacancy-centre-based quantum processor¹⁶, and FT parity-check measurements³⁵ and repetitive rounds of FT QEC cycles¹⁵ with trapped ions. In this study, alongside the operation of single-qubit logical Clifford gates, we demonstrate the FT implementation of a logical controlled-NOT (CNOT) gate between two logical colour-code qubits, thereby realizing the entire Clifford group fault-tolerantly. As this is all one can hope for regarding transversal implementations, to obtain the non-Clifford gate required for universality, we amend the gate set by a T gate. For this, in a first step we prepare a magic state fault-tolerantly by the use of flag qubits, as proposed in ref. 8. Finally, using this fault-tolerantly prepared magic state and the transversal logical CNOT gate, we perform FT magic-state injection, thus demonstrating a universal FT gate set.

We work with the seven-qubit colour code, illustrated in Fig. 1a, which is the smallest member of the code family of topological two-dimensional colour codes¹¹ and is also known as the Steane code¹². It hosts one logical qubit and can be formulated as a stabilizer code on seven physical qubits, with logical states encoded in the joint +1 eigenspace of six weight-four Pauli operators. The logical operators are $X_L = X^{\otimes 7}$ and $Z_L = Z^{\otimes 7}$, which are stabilizer-equivalent to weight-three operators, for example, $Z_L \approx Z_1 Z_2 Z_3$, rendering it a distance-three code. This entails that all single-qubit errors can be corrected, but weight-two errors on the code will lead to logical failures. Besides a transversal CNOT gate, remarkably it also admits the transversal implementation of the Hadamard gate H and the phase gate S . Consequently the entire Clifford group can be implemented transversally (Fig. 1b)¹. The required magic resource state to enable T -gate injection can be prepared fault-tolerantly owing to a recently proposed protocol⁸.

The experiments presented in this study have been performed in a 16-qubit ion-trap quantum information processor³⁶ shown schematically in Fig. 1c. The native gate set is composed of entangling Mølmer-Sørensen operations³⁷ and single-qubit rotations around an arbitrary axis in the equatorial plane of the Bloch sphere with error rates of $p_2 = 2.5 \times 10^{-2}$ and $p_1 = 5 \times 10^{-3}$, respectively. Error rates for state initialization and measurement are estimated at $p_i = 3 \times 10^{-3}$ and $p_m = 3 \times 10^{-3}$, respectively. A more detailed discussion on the experimental setup can be found in Methods. For better readability, all circuits shown in this study are provided in standard CNOT gates, as these are equivalent to Mølmer-Sørensen gates up to local Clifford operations³⁸. All experimental results are accompanied by Monte Carlo simulations, for which we model imperfections as uniform depolarizing noise on single-qubit gates, initialization and measurement as well as two-qubit gates with independent physical error rates p_i , p_p , p_m and p_2 , respectively, as described in Methods.

Initializing and characterizing the logical qubit

We start by experimentally preparing the logical state $|0\rangle_L$ as the +1 eigenstate of the logical Z operator Z_L by implementing the circuit

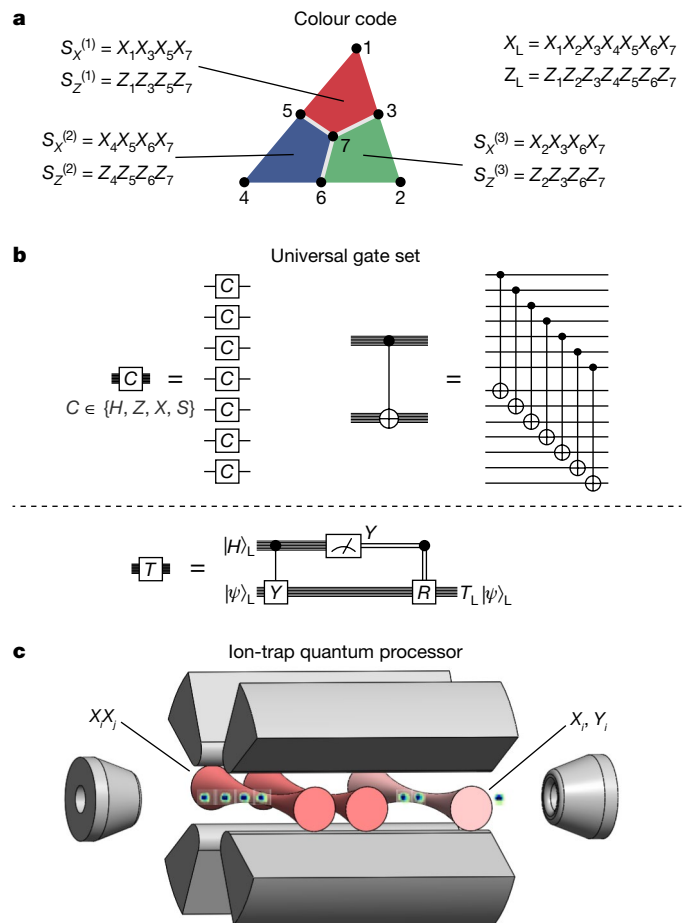
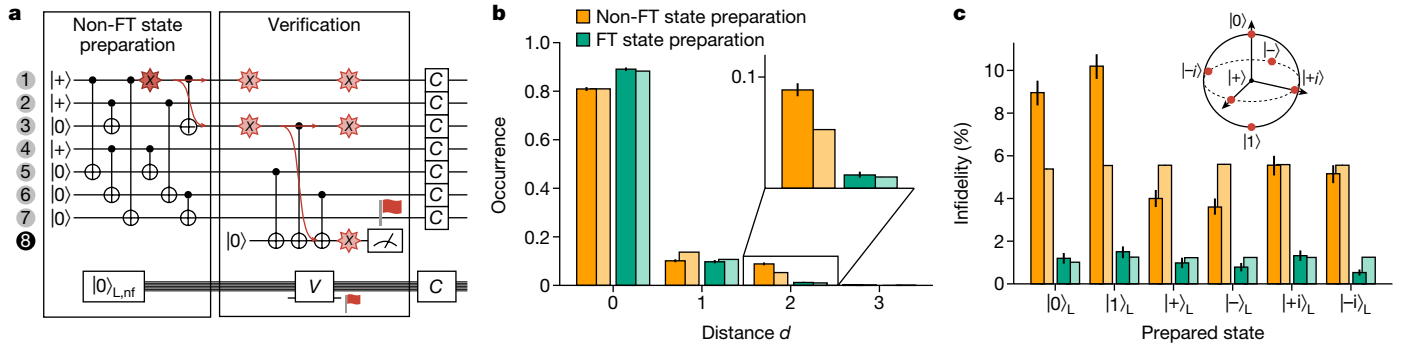


Fig. 1 | Quantum error-correction code, logical gates and experimental system. **a**, Seven-qubit colour code encoding one logical qubit in seven physical qubits. The six weight-four operators $\{S_X^{(i)}, S_Z^{(i)}\}$, where $i = 1, 2$ or 3 , are the stabilizer generators and the weight-seven operators are logical operators Z_L and X_L . **b**, Universal gate set consisting of Clifford gates (above dashed line) and the T gate. Whereas the Clifford group is transversal in the colour code, magic-state injection can be used to realize the FT T gate. The magic state $|H\rangle_L$ is prepared fault-tolerantly and subsequently teleported onto the target qubit in an arbitrary state $|\psi\rangle_L$, effectively implementing a T gate on the target qubit. **c**, Schematic three-dimensional model of the ion-trap quantum processor. Single ions and any pair of ions i and j can be addressed simultaneously by steerable tightly focused laser beams. This enables entangling (darker shaded beams) but also single-qubit (lighter) gates.

shown in Fig. 2a. The first part of the circuit encodes a logical qubit in a non-FT fashion. To render this encoding circuit FT, a verification step is added (Fig. 2a)^{13,39}. An additional auxiliary qubit is used to herald a successful logical qubit initialization, meaning that for a measurement outcome of +1, no single error anywhere in the encoding circuit can have led to uncorrectable errors on the data qubit register. For a measurement outcome of −1 of the flag qubit, the initialization is aborted and repeated.

We analyse the quality of the information encoded in a logical qubit in terms of logical operator expectation values. After a projective measurement, the outcome of the logical operators is corrected according to the measured error syndrome, effectively performing a Pauli frame update^{40,41} described in Methods. The updated measurement outcomes are categorized by their minimum Hamming distance d to any constituent state of the logical zero state (Methods) of zero, one, two and three. For outcomes with a minimum Hamming distance of zero or one, the logical state is recoverable, whereas for distances two and three, an



be applied. **b**, Relative occurrence rates of logical output states of distance d to the target state $|0\rangle_L$ for non-FT (orange) and FT (turquoise) initialization. Example states of $d=1$, $d=2$ and $d=3$ are $X_0|0\rangle_L$, $X_0X_1|0\rangle_L$ and $X_0X_1X_2|0\rangle_L$. Simulation results are depicted by lighter coloured bars. As described in the main text, all circuit elements are subject to depolarizing noise in numerical simulations. **c**, Logical infidelities of all six logical Pauli eigenstates (red markers on Bloch sphere) including an ideal round of error correction performed in post-processing (experimental and simulation results depicted darker and lighter, respectively).

uncorrectable logical error is induced. The relative occurrence of outcomes associated with those four categories for the initialization of $|0\rangle_L$ is shown in Fig. 2b. The verification circuit significantly suppresses the occurrence of errors leading to logical errors, resulting in decreased relative occurrences for outcomes with distances two and three by a factor of more than seven. A figure of merit describing the quality of the encoded state is the logical state fidelity, that is, the overlap of the measured with the target logical Bloch vector (Methods). The logical infidelity is decreased from 0.090(6) to 0.012(2) by introducing the verification of the initialization, showing a clear signature that an FT implementation outperforms its non-FT counterpart. The acceptance rate heralded by a +1 outcome of the flag measurement is 78.9(5)%. This behaviour is in good qualitative agreement with numerical simulations, which yield infidelities of 0.0538(2) and 0.0101(1) for the non-FT and FT circuits respectively, and an acceptance rate of 84.42(4)%.

Transversal fault-tolerant operations

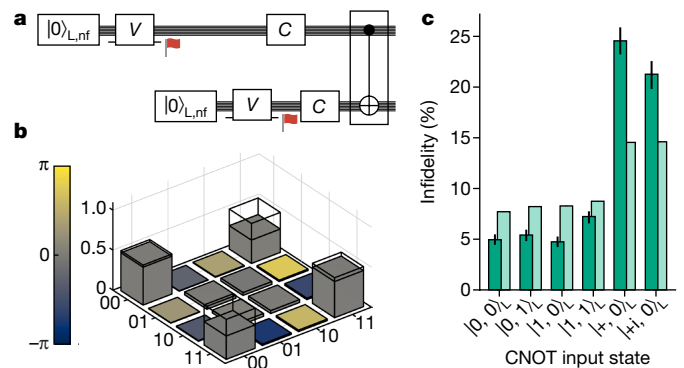
The transversality of the Clifford group as a property of the colour code allows for the preparation of the six cardinal states on the Bloch sphere, referred to as Pauli eigenstates herein, by applying single-qubit rotations corresponding to the respective logical gate to all qubits in the data register (Fig. 1b). For both the experimental data and the results of numerical simulations, the verification of the initialization reduces the logical infidelity of all six Pauli eigenstates, as can be seen in Fig. 2c. The definition of the logical fidelity and a discussion on the variation of the logical infidelity for different Pauli eigenstates can be found in the Methods. The average logical infidelity for the FT circuit is 0.011(1) with an acceptance rate of 80.6(2)%, whereas simulations suggest an average infidelity of 0.01203(4). The six stabilizer generators were measured projectively to verify the preparation of the correct encoded states for the Pauli states. The averaged expectation value of the X -type (Z -type) stabilizers is 0.826(3) (0.760(3)) for the FT preparation scheme and 0.842(3) (0.790(3)) for the non-FT preparation scheme. Further details on the measured stabilizer generators can be found in 'Logical Pauli states' in the Methods.

In Fig. 3, the implementation of a two-qubit gate acting on two logical qubits prepared as described above, requiring 29 entangling gates on 16 qubits, is illustrated. The transversal logical CNOT gate is implemented by sequentially applying CNOT gates to corresponding pairs of physical qubits of the two logical qubits (Fig. 1b). A single error on any of the physical qubits propagates to at most one error on each of

the logical qubits and therefore remains correctable, thereby ensuring fault tolerance of the gate realization. Applying the logical CNOT gate to the input state $|+\rangle, |0\rangle_L$ yields the logical Bell state $\frac{1}{\sqrt{2}}(|0, 0\rangle_L + |1, 1\rangle_L)$ depicted in Fig. 3b, showing a logical fidelity of 0.754(13) (Methods). Figure 3c shows the logical infidelity for six different input states. It reveals that the infidelity of output states is higher if the control qubit is in a superposition state, thus leading to an entangled outcome, compared with cases in which the outcome is a basis state of the logical two-qubit computational basis. This increased error rate is well described by numerical simulations based on the circuit noise model: the average logical infidelity is 0.110⁺³₋₂ and 0.1035(1) for the experimental implementation and the numerical simulation, respectively.

Universal fault-tolerant operations

The ability to perform a $\pi/4$ rotation about any axis is known to be sufficient to augment the set of Clifford gates, which are transversal in the colour code, to a universal gate set. The logical T gate



be applied. **b**, Relative occurrence rates of logical output states of distance d to the target state $|0\rangle_L$ for non-FT (orange) and FT (turquoise) initialization. Example states of $d=1$, $d=2$ and $d=3$ are $X_0|0\rangle_L$, $X_0X_1|0\rangle_L$ and $X_0X_1X_2|0\rangle_L$. Simulation results are depicted by lighter coloured bars. As described in the main text, all circuit elements are subject to depolarizing noise in numerical simulations. **c**, Logical infidelities of all six logical Pauli eigenstates (red markers on Bloch sphere) including an ideal round of error correction performed in post-processing (experimental and simulation results depicted darker and lighter, respectively).

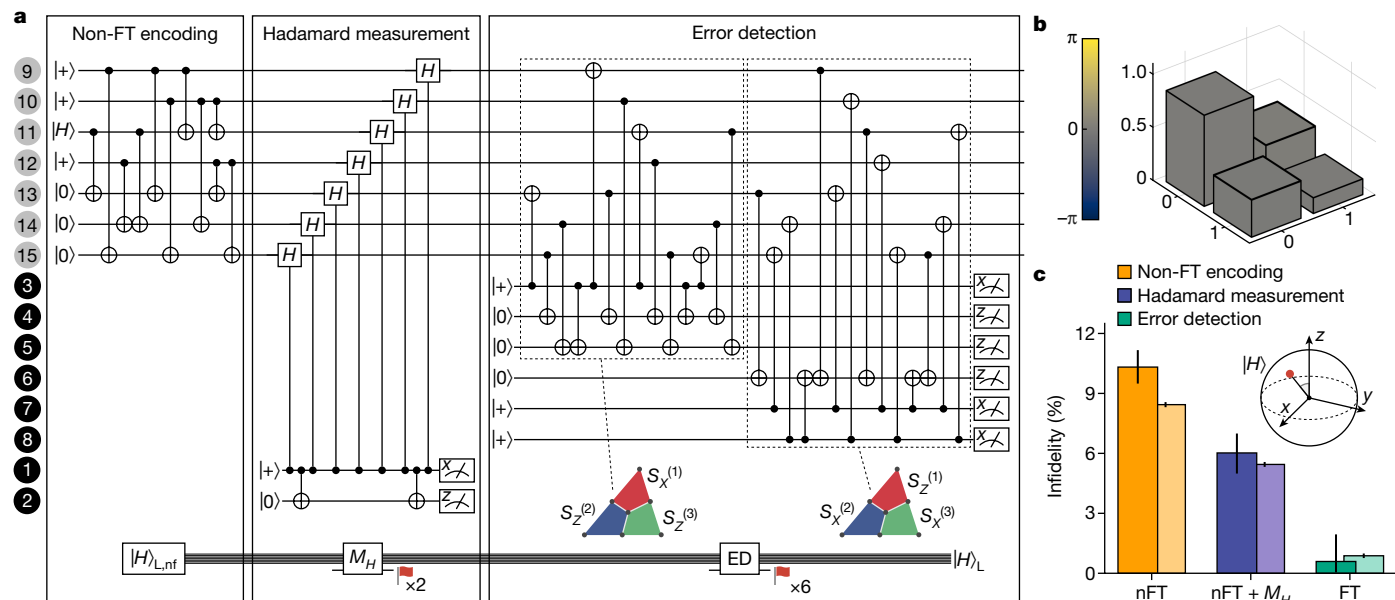


Fig. 4 | Fault-tolerant generation of a logical magic state $|H\rangle_L$. **a**, The magic state is prepared non-fault-tolerantly in a first step, where a physical magic state $|H\rangle$ is mapped to the logical state $|H\rangle_{L,nf}$ encoded in the data qubits at positions 9 to 15 in the ion string (see labels at left of circuit). Thereafter, a FT measurement of the Hadamard operator (M_H) is carried out. Two auxiliary qubits herald that the prepared state is a +1 eigenstate of the Hadamard operator but also that no dangerous error occurred during the measurement. The magic-state preparation is concluded with an error-detection (ED) block that measures the three X-type and Z-type stabilizers each in an FT fashion. The first part of the error-detection circuit (first dashed box), measures $S_X^{(1)}$, $S_Z^{(2)}$ and $S_Z^{(3)}$, whereas the second part measures $S_X^{(2)}$, $S_X^{(3)}$ and $S_X^{(1)}$. The magic-state

preparation is discarded and repeated in case of a non-trivial syndrome of the eight auxiliary qubits 1 to 8. **b**, Logical state tomography (see ‘Transversal fault-tolerant operations’) after FT magic-state preparation. The phase of the complex amplitudes is encoded in the colour of the three-dimensional bar plot and the wireframes depict ideal results. Phase deviations from the ideal density matrix are smaller than 50 mrad whereas amplitude deviations are smaller than 0.007. **c**, The decrease in infidelity of the logical magic state (red marker on Bloch sphere) after each step of the FT preparation procedure is observed experimentally and captured by depolarizing noise simulations (experimental and simulation results depicted darker and lighter, respectively).

$$T_L = e^{-i\frac{\pi}{8}Y_L} \quad (1)$$

performs a $\pi/4$ rotation about the y axis (it is noted that choosing this rotation axis is Clifford-equivalent to the more conventional T gate where the $\pi/4$ rotation is performed about the z axis) and can be implemented by magic-state injection as shown in Fig. 1b. It consists of the logical CNOT operation we have demonstrated in the preceding section, a logical measurement and single-qubit Clifford operation conditioned on the logical measurement outcome. First preparing and then injecting the logical magic state

$$|H\rangle_L = \cos(\pi/8)|0\rangle_L + \sin(\pi/8)|1\rangle_L \quad (2)$$

enables gate teleportation of the logical non-Clifford T gate. The logical magic state in equation (2) is the +1 eigenstate of the logical Hadamard operator.

Recently, a resource-efficient procedure to prepare a magic state using FT circuits following the flag-fault-tolerance paradigm has been proposed^{8,13}. The procedure consists of the following steps, depicted in Fig. 4a: we begin with a non-FT preparation of the magic state $|H\rangle_{L,nf}$, as recently demonstrated also in ref.¹⁵ (shown in the ‘Non-FT encoding’ box). Next, a measurement of the logical Hadamard operator is performed, which projects input states onto the +1 eigenspace and discards states that are eigenstates with eigenvalue -1 (‘Hadamard measurement’ box). The latter may be caused by single faults in the circuit (for example, faults in the initial state preparation of $|H\rangle$ for physical qubit 11), thus rendering the circuit non-FT if -1 eigenstates are not discarded in this step. Here both auxiliary qubits (qubits 1 and 2) are utilized as flag qubits. The syndrome measurement auxiliary qubit flags when the -1

eigenstate has erroneously been prepared, and the second auxiliary qubit flags when a dangerous fault has occurred that may corrupt the state. The last step is a complete error-correction (EC) cycle, consisting of fault-tolerantly measuring all six stabilizers of the colour code using one flag qubit per stabilizer as suggested in ref.⁶. The EC block is used to sort out faulty states whenever any flag qubit is measured as -1 and thus enables error detection (‘Error detection’ box). The resulting states after performing all three steps are guaranteed to be the correct logical magic state $|H\rangle_L$ up to correctable single-qubit errors provided at most one fault has occurred anywhere in the circuit. The generated state is accepted as valid if all eight flag qubits indicate that no harmful error has happened.

In Fig. 4b, the reconstructed density matrix of the fault-tolerantly prepared magic state is shown and its ideal numerical values can be found in Methods. We note that in the experiment we prepared the magic state up to local operations, which we account for in post-processing. See Methods for further details. Figure 4c shows the logical infidelity of the magic state, which clearly decreases after each preparation step in both experiment and simulation. Each step of the magic-state initialization process improves the quality of the generated logical state. After the full FT initialization procedure, a logical infidelity of $0.006_{-5}^{+14}\%$ for the magic state $|H\rangle_L$ with an acceptance rate of 13.7(3)% is found in the experimental realization, whereas numerical simulations predict approximately 27% (see Methods for discussion).

Next, the FT magic-state initialization is followed by transversal Clifford operations to fault-tolerantly teleport the logical magic state, thereby resulting in a realization of a FT logical T gate. For this, we perform an in-sequence measurement of the flag qubits for the magic-state generation as sketched in Fig. 5a. In the case of heralded successful magic-state generation, the auxiliary qubits are in a well defined state

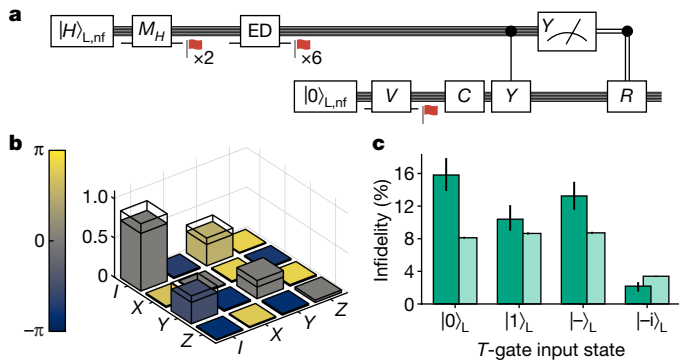


Fig. 5 | Fault-tolerant T -gate injection. **a**, After preparing the logical magic state fault-tolerantly, the logical T gate is applied via logical gate teleportation onto a second register that has a logical Pauli state prepared. Conditional application of $R \equiv R_y(\pi/2)$ is done in post-processing. **b**, Logical process matrix of the experimental logical T gate. The phase of the complex amplitudes is encoded in the colour of the three-dimensional bar plot and the wireframes depict ideal results. **c**, Infidelities of the data qubit state when applying the logical T gate to several logical Pauli input states (experimental and simulation results depicted darker and lighter, respectively). Infidelity is the lowest for the $|-i\rangle_L$ state as it is an eigenstate of the T gate.

after the measurement and can directly be re-used to encode a second logical qubit in $|0\rangle_L$ using the FT protocol from Fig. 2a. We then apply a transversal Clifford operation on this second logical qubit to prepare one of the logical initial states $|0\rangle_L, |1\rangle_L, |-\rangle_L$ or $|-i\rangle_L$. Finally, the transversal controlled- Y operation is applied on the second register and all physical qubits are measured. The measurement outcome for the logical Y operator of the control qubit in the first register is then extracted and the conditional $Y(\pi/2)$ rotation R to the target qubit in the second register is applied in post-processing (see Methods for details). By measuring the logical state of the target register for the four different initial states, it is possible to reconstruct the logical process matrix, shown in Fig. 5b with the ideal values explained in Methods. Figure 5c shows the logical infidelities for the different input states, yielding a mean infidelity of 0.10(1). It is expected and indeed observed experimentally that the best fidelity is achieved for the logical Y eigenstate $|-i\rangle_L$ as it is an eigenstate of the T gate. Infidelities for the three other logical input states are slightly higher, which qualitatively agrees with the numerical simulations.

Discussion and outlook

In this work, we have demonstrated the FT implementation of a universal set of single- and two-qubit logical gates. We were able to witness a hallmark feature of FT circuit design, namely, an improvement in the performance of encoded qubits, despite the FT implementations of encoding and manipulation requiring an increased gate count and the complexity of the underlying circuits. The resource-efficient implementation of these FT operations is enabled by the all-to-all qubit connectivity in the present trapped ion architecture, allowing for entangling operations between arbitrary pairs of qubits. Predictions from numerical simulations based on a relatively simple, generic and architecture-agnostic depolarizing circuit noise model, only informed by estimated experimental error rates, approximate the experimental findings well. The largest deviations between experimental behaviour and numerical predictions were observed for the logical CNOT gate. A more extensive characterization of this logical entangling gate and the other FT gadgets, together with more sophisticated and validated theoretical noise models will be subject to future investigations, and is imperative for designing future QEC architectures and procedures.

On the way towards error-protected universal quantum computation on even more robust logical qubits, further milestones ahead are the incorporation of repetitive QEC cycles^{15,42} into the FT logical gate operations demonstrated in our work. Another hurdle to be taken is the demonstration of error correction and FT gate operations for larger-distance logical qubits⁸.

Online content

Any methods, additional references, Nature Research reporting summaries, source data, extended data, supplementary information, acknowledgements, peer review information; details of author contributions and competing interests; and statements of data and code availability are available at <https://doi.org/10.1038/s41586-022-04721-1>.

- Nielsen, M. A. & Chuang, I. L. *Quantum Computation and Quantum Information: 10th Anniversary Edition* (Cambridge Univ. Press, 2010).
- Terhal, B. M. Quantum error correction for quantum memories. *Rev. Mod. Phys.* **87**, 307–346 (2015).
- Shor, P. W. Fault-tolerant quantum computation. In *Proc. 37th Conference on Foundations of Computer Science* 56–65 (IEEE, 1996).
- Preskill, J. Reliable quantum computers. *Proc. R. Soc. Lond. A* **454**, 385–410 (1998).
- Aliferis, P., Gottesman, D. & Preskill, J. Quantum accuracy threshold for concatenated distance-3 codes. *Quantum Inf. Comput.* **6**, 97–165 (2006).
- Chao, R. & Reichardt, B. W. Quantum error correction with only two extra qubits. *Phys. Rev. Lett.* **121**, 050502 (2018).
- Chamberland, C. & Beverland, M. E. Flag fault-tolerant error correction with arbitrary distance codes. *Quantum* **2**, 53 (2018).
- Chamberland, C. & Cross, A. W. Fault-tolerant magic state preparation with flag qubits. *Quantum* **3**, 143 (2019).
- Chao, R. & Reichardt, B. W. Flag fault-tolerant error correction for any stabilizer code. *PRX Quantum* **1**, 010302 (2020).
- Reichardt, B. W. Fault-tolerant quantum error correction for Steane's seven-qubit color code with few or no extra qubits. *Quantum Sci. Technol.* **6**, 015007 (2020).
- Bombin, H. & Martin-Delgado, M. A. Topological quantum distillation. *Phys. Rev. Lett.* **97**, 180501 (2006).
- Steane, A. Multiple-particle interference and quantum error correction. *Proc. R. Soc. Lond. A* **452**, 2551–2577 (1996).
- Goto, H. Minimizing resource overheads for fault-tolerant preparation of encoded states of the Steane code. *Sci. Rep.* **6**, 19578 (2016).
- Bravyi, S. & Kitaev, A. Universal quantum computation with ideal Clifford gates and noisy ancillas. *Phys. Rev. A* **71**, 022316 (2005).
- Ryan-Anderson, C. et al. Realization of real-time fault-tolerant quantum error correction. *Phys. Rev. X* **11**, 041058 (2021).
- Abobeih, M. H. et al. Fault-tolerant operation of a logical qubit in a diamond quantum processor. Preprint at <https://arxiv.org/abs/2108.01646> (2021).
- Shor, P. W. Polynomial-time algorithms for prime factorization and discrete logarithms on a quantum computer. *SIAM J. Comput.* **26**, 1484–1509 (1997).
- Feynman, R. P. Simulating physics with computers. *Int. J. Theor. Phys.* **21**, 467–488 (1982).
- Aharonov, D. & Ben-Or, M. Fault-tolerant quantum computation with constant error rate. *SIAM J. Comput.* **38**, 1207–1282 (2008).
- Eastin, B. & Knill, E. Restrictions on transversal encoded quantum gate sets. *Phys. Rev. Lett.* **102**, 110502 (2009).
- Paetzold, A. & Reichardt, B. W. Universal fault-tolerant quantum computation with only transversal gates and error correction. *Phys. Rev. Lett.* **111**, 090505 (2013).
- Beverland, M. E., Kubica, A. & Svore, K. M. Cost of universality: a comparative study of the overhead of state distillation and code switching with color codes. *PRX Quantum* **2**, 020341 (2021).
- Nigg, D. et al. Quantum computations on a topologically encoded qubit. *Science* **345**, 302–305 (2014).
- Harper, R. & Flammia, S. T. Fault-tolerant logical gates in the IBM quantum experience. *Phys. Rev. Lett.* **122**, 080504 (2019).
- Erhard, A. et al. Entangling logical qubits with lattice surgery. *Nature* **589**, 220–224 (2021).
- Satzinger, K. J. et al. Realizing topologically ordered states on a quantum processor. *Science* **374**, 1237–1241 (2021).
- Andersen, C. K. et al. Repeated quantum error detection in a surface code. *Nat. Phys.* **16**, 875–880 (2020).
- Marques, J. F. et al. Logical-qubit operations in an error-detecting surface code. *Nat. Phys.* **18**, 80–86 (2021).
- Chen, Z. et al. Exponential suppression of bit or phase errors with cyclic error correction. *Nature* **595**, 383–387 (2021).
- Gottesman, D. Quantum fault tolerance in small experiments. Preprint at <https://arxiv.org/abs/1610.03507> (2016).
- Takita, M., Cross, A. W., Córcoles, A. D., Chow, J. M. & Gambetta, J. M. Experimental demonstration of fault-tolerant state preparation with superconducting qubits. *Phys. Rev. Lett.* **119**, 180501 (2017).
- Vuillot, C. Is error detection helpful on IBM 5Q chips? *Quantum Inf. Comput.* **18**, 949–964 (2018).
- Linke, N. M. et al. Fault-tolerant quantum error detection. *Sci. Adv.* **3**, e1701074 (2017).

34. Egan, L. et al. Fault-tolerant control of an error-corrected qubit. *Nature* **598**, 281–286 (2021).
 35. Hilder, J. et al. Fault-tolerant parity readout on a shuttling-based trapped-ion quantum computer. *Phys. Rev. X* **12**, 011032 (2022).
 36. Pogorelov, I. et al. Compact ion-trap quantum computing demonstrator. *PRX Quantum* **2**, 020343 (2021).
 37. Sørensen, A. & Mølmer, K. Entanglement and quantum computation with ions in thermal motion. *Phys. Rev. A* **62**, 022311 (2000).
 38. Nebendahl, V., Häffner, H. & Roos, C. F. Optimal control of entangling operations for trapped-ion quantum computing. *Phys. Rev. A* **79**, 012312 (2009).
 39. Bermudez, A., Xu, X., Gutiérrez, M., Benjamin, S. C. & Müller, M. Fault-tolerant protection of near-term trapped-ion topological qubits under realistic noise sources. *Phys. Rev. A* **100**, 062307 (2019).
 40. Riesebo, L., Fu, X., Varsamopoulos, S., Almudever, C. G. & Bertels, K. Pauli frames for quantum computer architectures. In *DAC '17: Proc. 54th Annual Design Automation Conference 2017* 1–6 (Association for Computing Machinery, 2017).
 41. Knill, E. Quantum computing with realistically noisy devices. *Nature* **434**, 39–44 (2005).
 42. Parrado-Rodríguez, P., Ryan-Anderson, C., Bermudez, A. & Müller, M. Crosstalk suppression for fault-tolerant quantum error correction with trapped ions. *Quantum* **5**, 487 (2021).
- Publisher's note** Springer Nature remains neutral with regard to jurisdictional claims in published maps and institutional affiliations.
- © The Author(s), under exclusive licence to Springer Nature Limited 2022

Methods

Trapping and cooling

The experiments described in this work are performed on a trapped-ion quantum computer.⁴⁰ Ca^+ ions are trapped in a macroscopic Paul trap and the optical qubit is encoded in two Zeeman sublevels of the $4S_{1/2}$ and $3D_{5/2}$ electronic states. Further details on the experimental setup can be found in a recent publication³⁶.

For this work, the ion crystal is configured to consist of 16 ions with an axial centre-of-mass (COM) mode frequency $\omega_{\text{ax,COM}} = 2\pi \times 400$ kHz and radial COM mode frequencies of $\omega_{\text{rad1,COM}} = 2\pi \times 3,270$ kHz and $\omega_{\text{rad2,COM}} = 2\pi \times 3,100$ kHz. Before executing any gate sequence, the radial motional modes of the ion chain are cooled nearly to the ground state via Doppler cooling for 2 ms, followed by resolved sideband cooling for 15 ms. Subsequently, the qubits are initialized via optical pumping to the $4S_{1/2, m_j=-1/2}$ ground state, where m_j is the z component of the total angular momentum.

Qubit manipulation

Coherent qubit manipulation is performed by individually addressable laser pulses at a wavelength of 729 nm. Pulses resonant with the $4S_{1/2, m_j=-1/2}$ to $3D_{5/2, m_j=-1/2}$ transition enable rotations around an arbitrary axis in the equatorial plane of the Bloch sphere, where the angle between the rotation axis and the x axis is determined by the phase ϕ of the light pulse. Those operations are described by $R_\phi^{(i)}(\theta) = \exp(-i\frac{\theta}{2}(\sigma_x^{(i)} \cos \phi - \sigma_y^{(i)} \sin \phi))$, where $\sigma_x^{(i)}$ and $\sigma_y^{(i)}$ are single-qubit Pauli matrices acting on qubit i and θ is the rotation angle. Rotations around the x -axis R_x (y -axis R_y) can be implemented by setting ϕ to 0 ($-\pi/2$). A pulse length of 15 μs is required to implement a $\pi/2$ pulse on a single qubit. Randomized benchmarking for single-qubit gates in the 16-ion chain yields an average fidelity of a $\pi/2$ gate of $99.51 \pm 0.05\%$. In addition, rotations around the z axis of the Bloch sphere for a specific ion can be implemented virtually by introducing a phase shift to all subsequent pulses applied to the ion.

Two-qubit gates are realized by the Mølmer-Sørensen interaction³⁷ described by $MS_{ij}(\theta) = \exp(-i\frac{\theta}{2}\sigma_x^{(i)}\sigma_x^{(j)})$. An arbitrary pair of ions is addressed with bichromatic beams slightly detuned from the radial COM mode $\omega_{\text{rad1,COM}}$. A gate time $t_{\text{gate}} = 270$ μs and detuning from the COM mode $\Delta \approx 2\pi \times 3.7$ kHz are chosen to allow for simultaneous decoupling of the two closest radial modes $\omega_{\text{rad1,COM}}$ and $\omega_{\text{rad1,2}}$ at the end of the interaction. An additional (third) frequency tone, 1.05 MHz blue-detuned from the carrier transition, compensates the a.c. Stark shift induced by the bichromatic light field. For $\theta = \pi/2$, this results in an XX gate, which is equivalent to a CNOT gate up to single-qubit rotations⁴³. A decomposition of a CNOT gate acting on qubits i and j into an XX gate and local operations with a freely selectable parameter $\nu = \pm 1$ is the following:

$$\text{CNOT}_{ij} = R_y^{(i)}(-\nu\pi/2) \cdot R_x^{(i)}(\pi/2) \cdot R_x^{(j)}(\nu\pi/2) \cdot MS_{ij}(-\pi/2) \cdot R_y^{(j)}(\nu\pi/2). \quad (3)$$

The average Bell-state fidelity in a chain of 16 ions is about 97.5% for entangling gates between neighbouring ions.

State readout

Qubit-state readout is performed by illuminating the ions with a light field resonant to the $4S_{1/2}$ -to- $4P_{1/2}$ transition and collecting the scattered photons. Owing to technical limitations imposed by the electron multiplying charge-coupled device (EMCCD) camera, site-resolved state readout is only possible after the coherent evolution. In-sequence detection events utilizing an avalanche photodiode (APD) can only reveal the number of excitations present in the ion string. A subset of qubits can be read out in-sequence by shelving the population in the $4S$ state of all other ions to the $3D_{5/2, m_j=-3/2}$ Zeeman sublevel before the illumination of the ion string with the detection light field. This

technique is used for the measurements presented in the ‘Universal fault-tolerant operations’ section. For the FT initialization of the magic state, the auxiliary qubits are measured via the APD. If there are no excited ions detected, the protocol is continued by reusing the measured ions for encoding a second logical qubit state and injecting the magic state. After an illumination time of 2 ms for the EMCCD measurement and 0.5 ms for the APD measurement, a readout fidelity of $>99.7\%$ is achieved, where this number refers to the single-qubit readout fidelity for EMCCD measurements and the discrimination between 0 and >0 excited qubits for APD measurements.

If the qubit manipulation is supposed to be continued after a detection event that scattered photons, meaning that a qubit was projected to the S state, in-sequence recooling is required as the scattered photons heat the ion chain, which would prevent subsequent gate operations with high fidelity. The experimental setup we used to conduct the experiments presented in this work at present does not support in-sequence cooling, therefore preventing the implementation of repeated rounds of error correction. We note that upgrades to the setup facilitating in-sequence cooling are about to be carried out and that in-sequence detection and recooling were already implemented in a different recent experiment of the research group⁴⁴.

Error estimation

The errors given throughout this paper solely account for statistical errors. For the estimation of the statistical fluctuations, all measured outcomes are resampled from a multinomial distribution according to their respective probabilities. The stated errors in the text and the error bars given in figures correspond to 68% confidence intervals extracted from the resampled datasets.

An additional source of errors is temporal fluctuations of the experimental performance owing to varying environmental parameters such as magnetic field or ambient temperature. Such fluctuations on the timescale of minutes to hours explain the increased logical infidelity of $|0\rangle_L$ and $|1\rangle_L$, compared with the other Pauli eigenstates in Fig. 2. In our experiment, the magnitude of these errors can exceed the contribution from statistical errors.

Simulation methods

Theoretical simulation results presented in the main text are obtained using stabilizer simulations and state-vector simulations for the logical Pauli states and magic-state preparation and injection circuits, respectively. We use the Performance Estimator of Codes On Surfaces (PECOS) package owing to its flexibility in analysing error propagation in different error models through Monte Carlo simulation (publicly available at <https://github.com/PECOS-packages/PECOS>)⁴⁵. In these simulations, any ideal circuit element is replaced by a faulty element, consisting of the ideal operation followed by an error operator, with a given probability.

We model circuit errors as depolarizing errors, which reproduces the experimentally observed infidelities well despite its conceptual simplicity, which does not take the microscopic physical processes underlying noisy gates and operations in the ion trap into account explicitly. Noise is applied in simulations by randomly placing Pauli errors E according to the experimental physical error rates after every single-qubit and two-qubit gate with their respective error rates p_1 and p_2 . These errors can be

$$E_1 \in \{\sigma_k, \forall k \in \{1, 2, 3\}\} \quad (4)$$

$$E_2 \in \{\sigma_k \otimes \sigma_l, \forall k, l \in \{0, 1, 2, 3\} \setminus \{I \otimes I\}\} \quad (5)$$

where $\sigma_k = \{I, X, Y, Z\}$ with $k = 0, 1, 2$ or 3 are the Pauli matrices and I is the identity operation. The error channels for our depolarizing noise model acting on a density matrix ρ read

$$\varepsilon_1(\rho) = (1 - p_1)\rho + \frac{p_1}{3}(\chi\rho\chi + Y\rho Y + Z\rho Z) \quad (6)$$

$$\varepsilon_2(\rho) = (1 - p_2)\rho + \frac{p_2}{15} \sum_{i=1}^{15} E_2^{(i)} \rho E_2^{(i)} \quad (7)$$

so that any single-qubit error is applied uniformly to the ideal gate with equal probability $p_1/3$ and the single-qubit gate is executed ideally with probability $1 - p_1$; two-qubit errors are applied uniformly after the ideal two-qubit gates with equal probability $p_2/15$ and any two-qubit gate is executed ideally with probability $1 - p_2$. The results of qubit initializations and measurements are flipped with respective probabilities p_i and p_m . In all simulations, we used physical error rates of

$$\begin{aligned} p_1 &= 0.005 \\ p_2 &= 0.025 \\ p_i &= p_m = 0.003 \end{aligned} \quad (8)$$

for the corresponding operations.

The logical Pauli state encoding circuits (Fig. 2a) and logical CNOT circuit (Fig. 3a) are simulated efficiently using stabilizer simulations. This is possible as we are preparing eigenstates of Pauli operators, measuring exclusively in one of three possible Pauli bases here and these circuits contain only Clifford gates.

This description as stabilizer states breaks down when arbitrary single-qubit rotations are to be performed by the circuit, especially with regards to the magic state (equation (2)), which generates the non-Clifford T gate. The circuits that fault-tolerantly prepare the logical magic state (Fig. 4a) and perform the gate teleportation (Fig. 5a) contain non-Clifford operations and thus we are required to run full state-vector simulations.

The Y -type teleportation circuit acts as follows on the Y -type magic state, as given by equation (2), and an arbitrary single-qubit input state $|\psi\rangle = \alpha|0\rangle + \beta|1\rangle$ with $\alpha, \beta \in \mathbb{C}$:

$$|H\rangle|\psi\rangle = (\cos(\pi/8)|0\rangle + \sin(\pi/8)|1\rangle)(\alpha|0\rangle + \beta|1\rangle) \quad (9)$$

$$\xrightarrow{\text{CY}} \cos(\pi/8)|0\rangle(\alpha|0\rangle + \beta|1\rangle) + i \sin(\pi/8)|1\rangle(\alpha|1\rangle - \beta|0\rangle) \quad (10)$$

$$= \frac{1}{\sqrt{2}} \left(|+\rangle \exp\left(-i\frac{\pi}{8}Y\right)|\psi\rangle + |-\rangle \exp\left(i\frac{\pi}{8}Y\right)|\psi\rangle \right) \quad (11)$$

$$= \frac{1}{\sqrt{2}} \left(|+\rangle T|\psi\rangle + |-\rangle \exp\left(i\frac{\pi}{4}Y\right)T|\psi\rangle \right) \quad (12)$$

where CY is the controlled- Y gate. Thus, in case of measuring the first qubit in the $|+\rangle$ state, the T gate is applied as desired to the state $|\psi\rangle$ on the second qubit. In the other case of a -1 measurement result of the first qubit in the Y basis, an additional Clifford operation, namely a $\pi/2$ rotation about the y axis, $\exp\left(-i\frac{\pi}{4}Y\right)$, must be applied to end up with the desired state $T|\psi\rangle$ on the second qubit.

Therefore, in the teleportation circuit (Fig. 5a), the logical controlled Y is followed by measurement of all data qubits of the first register in the Y basis and application of a classically controlled logical Y rotation

$$R \equiv R_Y(\pi/2) = \exp\left(-i\frac{\pi}{4}Y\right) \quad (13)$$

depending on the measurement result of the first register where the logical magic state has been prepared previously. The logical gate

$R_i \simeq R^{\otimes 7}$ is applied to the second register, which carries a logical Pauli state, for example, $|+\rangle_L$. The resulting output state is the logical T gate applied to the logical Pauli state, for example, $T_1|+\rangle_L$. Both in simulation and experiment, the effect of the R gate is taken into account by altering the destructive final data qubit measurements. As R is a $\pi/2$ rotation about the y axis, it maps Z -basis states onto X -basis states and vice versa.

In our experimental implementation of the magic state, we omitted a $Y(\pi/2)$ rotation. Therefore, we applied logical R in the case of the $+1$ outcome of the logical Y -basis measurement of the first register.

Ideal error correction

Whenever performing destructive measurements on encoded data qubits, we may reinterpret the measurement result according to the colour code look-up table decoder. For example, from measuring the bitstring 0000001 on a seven-qubit register, we may conclude for low physical error rates present in our setup that the likeliest error on those qubits has been a single X flip on the first qubit and reinterpret the measurement result as 0000000. This process of ideal or in-software EC is commonly used and possible whenever one aims not to keep running further quantum circuits on the error-corrected state. In general, the corrected bitstring is determined by extracting the syndrome from the overlap of the measured bitstring with the stabilizer generators in binary notation and applying the respective correction. For CSS (Calderbank–Shor–Steane) codes such as the colour code, the X and Z sectors can be treated distinctly. Therefore, when measuring the bitstring 0000001 in the Z basis, the overlap with Z stabilizers in binary notation $s_Z^{(1)} = 1010101$, $s_Z^{(2)} = 1111000$, $s_Z^{(3)} = 1100110$ yields the syndrome $[-1, +1, +1]$. Here binary 1s correspond to a Pauli Z operator for the single qubit at the respective position and binary 0s represent the identity operation. Reinterpreting the measured bitstring as 0000000 is equivalent to applying an X_1 correction operator based on the syndrome information, which would correctly recover the original state. As in this work we are demonstrating FT operations, all final quantum states may only be correct up to an arbitrary single Pauli error. These errors are accounted for via ideal error correction.

Logical Pauli states

When fault-tolerantly encoding logical Pauli states, we characterize the output state by categories of errors present after executing the circuit in Fig. 2a. The categories of errors given in Fig. 2b refer to the states of distance d to the desired $|0\rangle_L$ state, which determines whether or not we can correctly identify the state as $|0\rangle_L$ after ideal EC.

We obtain the distance d to the desired $|0\rangle_L$ state by destructively measuring the data qubit register and finding the minimal Hamming distance D_H of the measurement bitstring m to the bitstrings that label the basis states of

$$\begin{aligned} |0\rangle_L &= \frac{1}{\sqrt{8}} (|0000000\rangle + |1010101\rangle + |0110011\rangle \\ &\quad + |1100110\rangle + |0001111\rangle + |1011010\rangle \\ &\quad + |0111100\rangle + |1101001\rangle) \end{aligned} \quad (14)$$

in post-processing:

$$d \equiv \min(D_H(m, 0000000), D_H(m, 1010101), \dots, D_H(m, 1101001)). \quad (15)$$

Ideal EC will trivially correct the exact $|0\rangle_L$ state, that is, $d = 0$, and correct all states with single Pauli errors, for example, $X_2|0\rangle_L$ ($d = 1$). It will yield the logically flipped $|1\rangle_L$ result when acting on a state of distance $d = 2$ or $d = 3$ from $|0\rangle_L$, that is, $|0\rangle_L$ carrying two X errors or directly a weight-three logical bit flip X_L .

For arbitrary logical Pauli states, destructive measurements must be performed in their respective basis. However, only X (Z) errors are visible in the preparation of logical Z - (X -) basis states $|0\rangle_L, |1\rangle_L$ ($|\pm\rangle_L$).

It is noted that for all measurements on the characterization of logical Pauli states shown in Fig. 2 and Extended Data Fig. 1, an accidental redefinition of the rotation direction of physical single-qubit Y rotations is accounted for in post-processing. See Extended Data Fig. 1 for more details.

Logical fidelities

Single-qubit logical states. The logical fidelities presented in the main text are obtained by reconstructing the logical Bloch vector of the prepared state ρ and determining the overlap with the Bloch vector of a logical target state. Within the code space, the projector onto an ideal single-qubit logical target state $\rho_t = |t\rangle\langle t|_L$ is given by

$$P_t = \frac{1}{2}(I + O_t) \quad (16)$$

with O_t the logical operator that the target state $O_t|t\rangle_L = |t\rangle_L$ is the +1 eigenstate too. For the Pauli states considered in this work the projectors are

$$P_{0/1} = \frac{1}{2}(I \pm Z_L) \quad (17)$$

$$P_{\pm} = \frac{1}{2}(I \pm X_L) \quad (18)$$

$$P_{\pm i} = \frac{1}{2}(I \pm Y_L) \quad (19)$$

and logical fidelity of a prepared state ρ follows as

$$\mathcal{F}_t(\rho) = \langle P_t \rangle = \text{tr}(\rho P_t). \quad (20)$$

We emphasize that these logical fidelities are not equivalent to the full quantum state fidelities $\mathcal{F} = \text{tr}(\rho_t \rho)$ but are the probabilities to be able to correctly conclude which logical state was intended to be prepared or stored.

Combining equations (17)–(19) with the expression for the logical fidelity in equation (20), we can see that expectation values of logical Pauli operators O_t need to be determined to find the logical fidelities

$$\mathcal{F} = \frac{1}{2}(1 \pm \langle O_t \rangle) \text{ with } O_t \in \{X_L, Y_L, Z_L\}, \quad (21)$$

which, for example, evaluates to $\mathcal{F}_0 = \frac{1}{2}(1 + \langle Z_L \rangle)$ for the logical Pauli state $|0\rangle_L$. All six cardinal state logical fidelities are shown in Fig. 2c. We sample the expectation values of the logical Pauli operators by running stabilizer simulations of the respective preparation circuit $N = 10^6$ times followed by destructive measurement of all data qubits and ideal EC in the respective Pauli basis. The measurement result for a logical operator before EC is determined as $(-1)^{|m|}$ by the number of 1s in the measurement bitstring m modulo 2. Then a round of ideal EC as described in ‘Ideal error correction’ is performed to obtain the final measurement result. Measurement results from each run are averaged to obtain the expectation value of the respective logical operator.

Two-qubit logical states. To characterize the logical CNOT gate through stabilizer simulations, single logical qubit states $|x\rangle_L$ and $|y\rangle_L$ are prepared distinctly in two seven-qubit registers. The CNOT gate, acting $|x, y\rangle_L \mapsto |x, y \oplus x\rangle_L$ on the basis states labelled with $x, y \in \{0, 1\}$, flips the second bit (target) if the first bit (control) is in the 1 state. Thus, $|+, 0\rangle_L$ is mapped to the maximally entangled Bell state

$$|\Phi^+\rangle_L = \frac{1}{\sqrt{2}}(|0, 0\rangle_L + |1, 1\rangle_L), \quad (22)$$

which can equivalently be expressed by the logical density operator

$$\rho_{\Phi^+} = |\Phi^+\rangle\langle\Phi^+|_L \simeq \frac{1}{2} \begin{pmatrix} 1 & 0 & 0 & 1 \\ 0 & 0 & 0 & 0 \\ 0 & 0 & 0 & 0 \\ 1 & 0 & 0 & 1 \end{pmatrix} \quad (23)$$

where the matrix representation is in the logical two-qubit computational basis. The input–output mapping for the experimentally implemented input states is the following:

$$\begin{pmatrix} |0, 0\rangle_L & \rightarrow |0, 0\rangle_L \\ |0, 1\rangle_L & \rightarrow |0, 1\rangle_L \\ |1, 0\rangle_L & \rightarrow |1, 1\rangle_L \\ |1, 1\rangle_L & \rightarrow |1, 0\rangle_L \\ |+, 0\rangle_L & \rightarrow |\Phi^+\rangle_L \\ |+, 1\rangle_L & \rightarrow |\Phi^+\rangle_L \end{pmatrix} \quad (24)$$

Quantum state tomography has been performed to quantify experimental capabilities to obtain the logical Bell state described by this density matrix as shown in Fig. 3b. Expectation values of all logical two-qubit Pauli matrices including the identity are measured and subsequently maximum likelihood techniques are used to reconstruct the logical density operator⁴⁶. The Bell state is stabilized by the logical operators $Z_L^1 Z_L^2$ and $X_L^1 X_L^2$ where the superscripts 1 and 2 refer to the two logical qubits. Analogously, the CNOT maps input $|+, 0\rangle_L$ to the Y -basis maximally entangled state

$$|\Phi^{+i}\rangle_L = \frac{1}{\sqrt{2}}(|0, 0\rangle_L + i|1, 1\rangle_L). \quad (25)$$

Its stabilizers can be obtained by realizing that both states are related via a phase gate

$$|\Phi^{+i}\rangle = S_1 |\Phi^+\rangle \quad (26)$$

so by transforming the stabilizer generators of $|\Phi^+\rangle$ as

$$S_1 Z_1 Z_2 S_1^\dagger = Z_1 Z_2 \quad (27)$$

$$S_1 X_1 X_2 S_1^\dagger = Y_1 X_2 \quad (28)$$

we obtain the stabilizer generators of $|\Phi^{+i}\rangle$.

The projectors onto the logical two-qubit output states we wish to characterize are now given by the product of the projectors onto the simultaneous +1 eigenspace of the logical operators in both registers

$$P_{00} = (P_0 \otimes I)(I \otimes P_0) = \frac{1}{2}(I + Z_L^1) \frac{1}{2}(I + Z_L^2) \quad (29)$$

$$P_{01} = (P_0 \otimes I)(I \otimes P_1) = \frac{1}{2}(I + Z_L^1) \frac{1}{2}(I - Z_L^2) \quad (30)$$

$$P_{11} = (P_1 \otimes I)(I \otimes P_1) = \frac{1}{2}(I - Z_L^1) \frac{1}{2}(I - Z_L^2) \quad (31)$$

$$P_{10} = (P_1 \otimes I)(I \otimes P_0) = \frac{1}{2}(I - Z_L^1) \frac{1}{2}(I + Z_L^2) \quad (32)$$

$$P_{\Phi^+} = \frac{1}{2}(I + X_L^1 X_L^2) \frac{1}{2}(I + Z_L^1 Z_L^2) \quad (33)$$

$$P_{\Phi^{+i}} = \frac{1}{2}(I + Z_L^1 Z_L^2) \frac{1}{2}(I + Y_L^1 X_L^2) \quad (34)$$

Using equation (20), the logical fidelities for the output states of the logical CNOT gate follow as expectation values of the logical two-qubit state projectors as

$$\mathcal{F}_{00} = \frac{1}{4}(1 + \langle Z_L^1 \rangle + \langle Z_L^2 \rangle + \langle Z_L^1 Z_L^2 \rangle) \quad (35)$$

$$\mathcal{F}_{01} = \frac{1}{4}(1 + \langle Z_L^1 \rangle - \langle Z_L^2 \rangle - \langle Z_L^1 Z_L^2 \rangle) \quad (36)$$

$$\mathcal{F}_{11} = \frac{1}{4}(1 - \langle Z_L^1 \rangle - \langle Z_L^2 \rangle + \langle Z_L^1 Z_L^2 \rangle) \quad (37)$$

$$\mathcal{F}_{10} = \frac{1}{4}(1 - \langle Z_L^1 \rangle + \langle Z_L^2 \rangle - \langle Z_L^1 Z_L^2 \rangle) \quad (38)$$

$$\mathcal{F}_{\Phi^+} = \frac{1}{4}(1 + \langle X_L^1 X_L^2 \rangle - \langle Y_L^1 Y_L^2 \rangle + \langle Z_L^1 Z_L^2 \rangle) \quad (39)$$

$$\mathcal{F}_{\Phi^-} = \frac{1}{4}(1 + \langle Z_L^1 Z_L^2 \rangle + \langle X_L^1 Y_L^2 \rangle + \langle Y_L^1 X_L^2 \rangle) \quad (40)$$

and are shown in Fig. 3b as results of $N = 10^6$ stabilizer simulation runs of the logical CNOT circuit followed by destructive measurement of all data qubits and ideal EC in the respective Pauli basis. Averaging over measurement results for the logical operators yields their expectation value.

The logical magic state $|H\rangle_L$ may be denoted by the logical density operator

$$\rho_H = |H\rangle\langle H|_L \simeq \frac{1}{2} \begin{pmatrix} 1 + 1/\sqrt{2} & 1/\sqrt{2} \\ 1/\sqrt{2} & 1 - 1/\sqrt{2} \end{pmatrix} \quad (41)$$

where the matrix representation is in the logical computational basis. Quantum state tomography of the experimentally prepared logical magic state is shown compared with the theoretical values in equation (41) in Fig. 4b, where a logical $Y(\pi/2)$ rotation is applied after reconstruction to account for omitted local operations. The fidelity of the logical magic state as shown in Fig. 4c is given by

$$\mathcal{F}_H = \frac{1}{2} \left(1 + \frac{\langle X_L \rangle + \langle Z_L \rangle}{\sqrt{2}} \right) \quad (42)$$

as the logical magic state is the +1 eigenstate of the logical Hadamard operator $H_L |H\rangle_L = |H\rangle_L$ and its projector reads

$$P_H = \frac{1}{2}(I + H_L) = \frac{1}{2} \left(I + \frac{X_L + Z_L}{\sqrt{2}} \right). \quad (43)$$

When we inject the logical magic state onto logical Pauli states the result is the logical T gate applied to the previously prepared logical Pauli state

$$|\psi\rangle_{L,\text{out}} = T_L |t\rangle_{L,\text{in}}. \quad (44)$$

For the four different input logical Pauli states $|0\rangle_L, |1\rangle_L, |- \rangle_L$ and $|-i\rangle_L$, the output states are

$$|H\rangle_L = T_L |0\rangle_L \quad (45)$$

$$|-H\rangle_L = T_L |1\rangle_L \quad (46)$$

$$Z_L |H\rangle_L = T_L |- \rangle_L \quad (47)$$

$$|-i\rangle_L = T_L |-i\rangle_L \quad (48)$$

and their projectors read

$$P_{0/1} = \frac{1}{2}(I \pm H_L) = \frac{1}{2} \left(1 \pm \frac{X_L + Z_L}{\sqrt{2}} \right) \quad (49)$$

$$P_{\pm} = Z_L P_0 Z_L = \frac{1}{2} \left(1 - \frac{X_L - Z_L}{\sqrt{2}} \right) \quad (50)$$

$$P_{\pm i} = \frac{1}{2}(I - Y_L). \quad (51)$$

The respective logical T -gate output-state fidelities \mathcal{F}_t for input Pauli state $|t\rangle_L$ are then given by

$$\mathcal{F}_0 = \frac{1}{2} \left(1 + \frac{\langle X_L \rangle + \langle Z_L \rangle}{\sqrt{2}} \right) \quad (52)$$

$$\mathcal{F}_1 = \frac{1}{2} \left(1 - \frac{\langle X_L \rangle + \langle Z_L \rangle}{\sqrt{2}} \right) \quad (53)$$

$$\mathcal{F}_{-} = \frac{1}{2} \left(1 - \frac{\langle X_L \rangle - \langle Z_L \rangle}{\sqrt{2}} \right) \quad (54)$$

$$\mathcal{F}_{-i} = \frac{1}{2}(1 - \langle Y_L \rangle). \quad (55)$$

To estimate the expectation values of the logical operators occurring in the expressions for the fidelities given above, we run $N = 10^5$ state-vector simulations of the FT preparation and injection circuits. Each run is followed by destructive measurement in the respective Pauli basis and ideal EC that determines a measurement outcome of the logical Pauli operator. The expectation value is then calculated as the mean over all measurement outcomes.

The sampling uncertainty ε_L when sampling the expectation value of a logical Pauli operator O_L is $\varepsilon_L = \sqrt{\frac{\text{Var}(\langle O_L \rangle)}{N}}$ and is propagated to their respective fidelities by Gaussian error propagation.

Logical process matrix

Process matrices can be used to parameterize quantum channels

$$\mathcal{E}(\rho) = \sum_{n=0}^3 \sum_{m=0}^3 \chi_{mn} E_m \rho E_n^\dagger \quad (56)$$

in the quantum operations formalism. The process matrix χ for the logical T gate that we show in Fig. 5b is described by the quantum channel

$$\mathcal{E}(\rho) = T \rho T^\dagger = \sum_{n=0}^3 \sum_{m=0}^3 \chi_{mn} \sigma_m \rho \sigma_n \quad (57)$$

where we expand the channel in terms of the logical Pauli matrices. The matrix representation of χ in the logical Pauli basis reads

$$\chi = \frac{1}{2} \begin{pmatrix} 1 + 1/\sqrt{2} & 0 & i/\sqrt{2} & 0 \\ 0 & 0 & 0 & 0 \\ -i/\sqrt{2} & 0 & 1 - 1/\sqrt{2} & 0 \\ 0 & 0 & 0 & 0 \end{pmatrix}. \quad (58)$$

Measurements of expectation values of the logical Pauli basis for the T -gate input states $|0\rangle_L, |1\rangle_L, |- \rangle_L$ and $|-i\rangle_L$ form a tomographically complete set and allow for the reconstruction of the process matrix χ_{mn} (ref. ⁴⁶).

Acceptance rates

We define the acceptance rate as ratio of circuit runs where all flag qubits are measured as +1. The logical Pauli $|0\rangle_L$ state is fault-tolerantly encoded ($|0\rangle_{L,ft}$) using the circuit given in Fig. 2a, the logical magic state is prepared both by using the non-FT circuit followed by only the transversal Hadamard measurement ($|H\rangle_{L,nf}$ and M_H) and by using the full FT protocol ($|H\rangle_{L,nf}$) as given in Fig. 4a. Approximate acceptance rates in simulation and experiment are shown in Extended Data Table 1 for these three different encoding circuits alongside the respective number of qubits acting as flags and the number of gates. We observe that the relative deviation $\Delta\epsilon$ between Monte Carlo simulation and experimentally measured acceptance rates for the respective circuits increases with longer circuits and a higher number of flag qubits involved.

Data availability

The data underlying the findings of this work and the quantum circuits are available at <https://doi.org/10.5281/zenodo.6244536>.

Code availability

All codes used for data analysis are available from the corresponding author upon reasonable request.

43. Maslov, D. Basic circuit compilation techniques for an ion-trap quantum machine. *New J. Phys.* **19**, 023035 (2017).
44. Ringbauer, M. et al. A universal qudit quantum processor with trapped ions. Preprint at <https://arxiv.org/abs/2109.06903> (2021)
45. Ryan-Anderson, C. *Quantum Algorithms, Architecture, and Error Correction*. PhD thesis, The Univ. New Mexico (2018).

46. Hradil, Z., Řeháček, J., Fiurášek, J. & Ježek, M. in *Quantum State Estimation* 59–112 (Springer, 2004).

Acknowledgements We acknowledge support from the EU Quantum Technology Flagship grant AQTION under grant agreement number 820495, and by the US Army Research Office through grant number W911NF-21-1-0007; and funding by the Austrian Science Fund (FWF), through the SFB BeyondC (FWF project number F7109), by the Austrian Research Promotion Agency (FFG) contract 872766, and by the IQI GmbH. M. Ringbauer acknowledges funding from the European Union's Horizon 2020 research and innovation programme under the Marie Skłodowska-Curie grant agreement number 840450. M. Müller acknowledges support by the ERC Starting Grant QNets grant number 804247. S.H. acknowledges funding by the Deutsche Forschungsgemeinschaft (DFG, German Research Foundation) under Germany's Excellence Strategy 'Cluster of Excellence Matter and Light for Quantum Computing (ML4Q) EXC 2004/1' 390534769. The research is also based on work supported by the Office of the Director of National Intelligence (ODNI), Intelligence Advanced Research Projects Activity (IARPA), via the US Army Research Office grant number W911NF-16-1-0070. The views and conclusions contained herein are those of the authors and should not be interpreted as necessarily representing the official policies or endorsements, either expressed or implied, of the ODNI, IARPA or the US Government. The US Government is authorized to reproduce and distribute reprints for governmental purposes notwithstanding any copyright annotation thereon. Any opinions, findings, and conclusions or recommendations expressed in this material are those of the author(s) and do not necessarily reflect the view of the US Army Research Office.

Author contributions L.P., I.P. and T.F. carried out the experiments. L.P., I.P., T.F., M. Meth, C.D.M., R.S., M. Ringbauer, P.S. and T.M. contributed to the experimental setup. L.P. analysed the data. S.H. performed the numerical simulations. S.H., M. Rispler and M. Müller performed circuit analysis, characterization and theory modelling. L.P., S.H., I.P., M. Rispler, P.S. and M. Müller wrote the manuscript, with contributions from all authors. R.B., P.S., M. Müller and T.M. supervised the project.

Competing interests T.M., R.B. and T.F. are connected to Alpine Quantum Technologies, a commercially oriented quantum computing company.

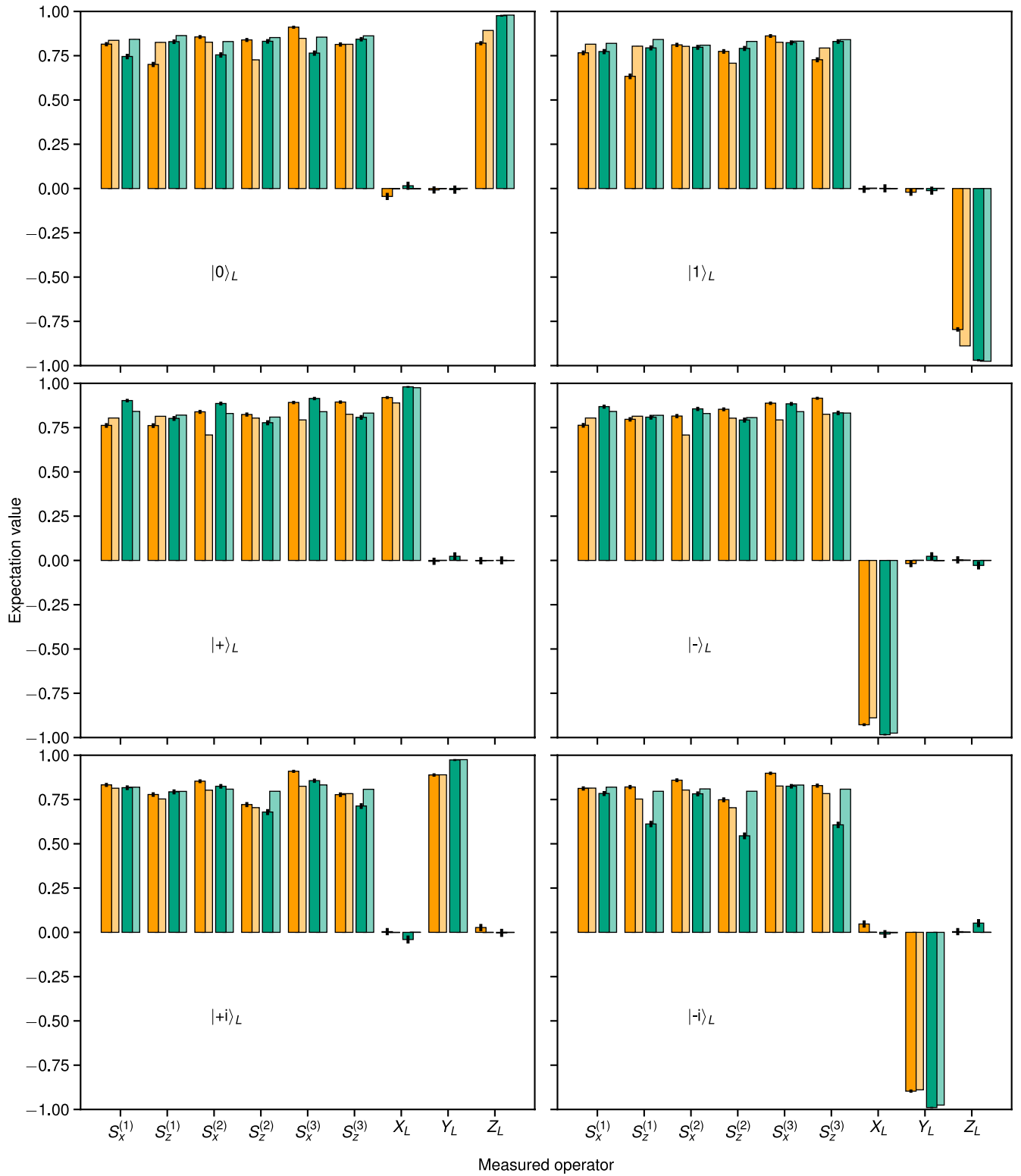
Additional information

Supplementary information The online version contains supplementary material available at <https://doi.org/10.1038/s41586-022-04721-1>.

Correspondence and requests for materials should be addressed to Philipp Schindler.

Peer review information *Nature* thanks the anonymous reviewers for their contribution to the peer review of this work. Peer reviewer reports are available.

Reprints and permissions information is available at <http://www.nature.com/reprints>.



Extended Data Fig. 1 | Stabilizer generators of a single logical qubit.

Expectation values of the stabilizer generators and the logical operators of the seven-qubit colour code for the six cardinal states of the Bloch sphere. Results for the non-fault-tolerant and fault-tolerant preparation scheme are depicted in orange and turquoise respectively, whereas results from numerical simulations are shown in lighter coloured bars. 2,500 and 10^6 runs were performed in the experiment and for simulations for each prepared state, respectively. For the calculation of the expectation values of the logical

operators a round of perfect error correction is applied. For the measurements corresponding to the data presented in this figure but also in Fig. 2 the sign of the rotation angle of physical Y-rotations is flipped, effectively implementing an additional deterministic π phase flip on qubit 6 and a π bit flip on qubit 7 at the end of the circuit depicted in Fig. 2a. The effects of this redefinition do not amount to a change of measurement bases and can be readily accounted for in post-processing.

Extended Data Table 1 | Acceptance rates of flag encoding circuits

encoding	#entangling gates	#flags	simulation	experiment	$\Delta\varepsilon$
$ 0\rangle_{L,\text{ft}}$	8	1	85%	79%	7%
$ H\rangle_{L,\text{nf}} \ \& \ M_H$	20	2	72%	57%	21%
$ H\rangle_{L,\text{ft}}$	48	8	27%	14%	48%

Approximate acceptance rates and relative deviation in simulation and experiment for three encoding circuits with different number of flag qubits and entangling gates.